13th International Symposium on Particle Image Velocimetry – ISPIV 2019
Munich, Germany, July 22-24, 2019

PIV Measurements under Reacting and Non-Reacting Conditions at the Nozzle Outlet of the SPP1980 SpraySyn Burner

Fabio J. W. A. Martins[1]*, Andreas Kronenburg[2] and Frank Beyrau[1]

[1] Institut für Strömungstechnik und Thermodynamik (ISUT),
Otto von Guericke University Magdeburg, Germany

[2] Institut für Technische Verbrennung, University of Stuttgart, Germany

* fabio.martins@ovgu.de

Abstract

Flame spray pyrolysis (FSP) has drawn the attention of the industry and scientific community due to its versatility, scalability and cost for synthesis of a wide variety of materials with controlled characteristics. Since the FSP processes are still not fully understood, standard burners have been developed for systematic experimental and numerical investigations. Within the DFG-funded Priority Programme on 'Nanoparticle Synthesis in Spray Flames SpraySyn: Measurement, Simulation, Processes' (SPP1980), a standard burner has been proposed. The characterization of the velocity field of this burner is therefore crucial, because the flow velocity is linked to the FSP processes, influencing the precursor atomization, flame and produced material. In the present work, we measure the gaseous velocity field from the nozzle outlet to positions located 26 mm downstream of the mentioned SpraySyn-burner by means of 2D-2C PIV at a variety of combinations of sheath-, pilot- and dispersion-gas flow rates under non-reacting and reacting conditions with different stoichiometry. The nozzle outlet velocity of the SpraySyn-burner is characterized by averages and standard deviations of PIV measurements.

1 Introduction

Flame spray pyrolysis (FSP) has demonstrated to be an attractive process to generate a wide spectrum of functional materials in the form of powders and films with tunable characteristics (Messing et al., 1993; Gurav et al., 1993; Mueller et al., 2003; Okuyama and Lenggoro, 2003; Strobel and Pratsinis, 2007; Kilian et al., 2014; Schulz et al., 2018). Countless products have been already synthesized from different precursor solutions by FSP processes, such as zinc oxide (ZnO), alumina (Al_2O_3), ceria (CeO_2), magnesia (MgO), magnesium-aluminate ($MgAl_2O_4$), cupric oxide (CuO), iron oxides (FeO, FeO_2, Fe_2O_3), titania (TiO_2), zirconia (ZrO_2), to name some (Mueller et al., 2003). Industry and scientific community have become interested in the FSP process because of the variety of potential applications, its flexibility, scalability and cost of production (Strobel and Pratsinis, 2007).

In the last 30 years, significant development in understanding of combustion aerosol formation has permitted FSP materials with nearly controlled characteristics to become available (Kilian et al., 2014; Schulz et al., 2018). After the liquid-precursor atomization, the particle formation by FSP can be described by several sequential physical-chemical mechanisms with branching connections that lead to a variety of different products (Gurav et al., 1993; Strobel and Pratsinis, 2007). For instance, for the formation of agglomerated fractal-like nano-particles the combined mechanisms are: droplet evaporation, precursor reaction (combustion), particle nucleation, surface growth, coagulation, sintering, aggregation and agglomeration (Strobel and Pratsinis, 2007). However, there is still a lack of knowledge of the complexity of the FSP process and the interplay between the particle-formation mechanisms, usually occurring within turbulent reacting multi-phase flow fields (Schulz et al., 2018).

To overcome this deficiency, standard burners allow for systematic experimental and numerical investigations. Different standard burners have been used for flame research, such as Hencken burner, Gülder

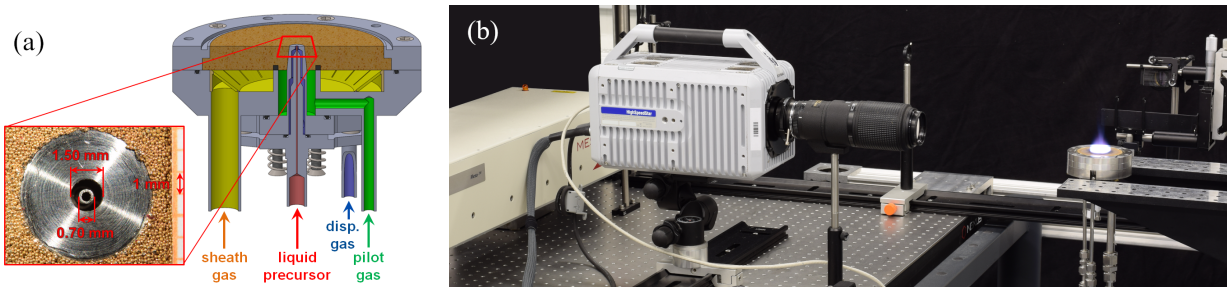

Figure 1: (a) Schematic cross-section of the SPP1980 SraySyn burner with zoomed image from the top of the nozzle outlet. (b) PIV experimental setup showing a premixed flat flame.

burner, Santoro burner, McKenna burner, Sandia Flame D, Cambridge swirl burner, CORIA spray burner, to name a few (Abdelsamie and Thévenin, 2019; Schneider et al., 2019). These burners can be operated under reproducible standard conditions to provide valuable databases (benchmarks) for understanding the underlying physics and to validate models. Within the DFG-funded Priority Programme on 'Nanoparticle Synthesis in Spray Flames SpraySyn: Measurement, Simulation, Processes' (SPP1980), a standard laboratory-scale spray-flame burner for nanoparticle synthesis has been proposed, called SpraySyn burner (Menser et al., 2014; Schneider et al., 2019).

The working principle of the SPP1980 SpraySyn-burner (Fig. 1a) is described as follows. The liquid precursors are atomized by a high-velocity oxygen dispersion gas, flowing through a central two-fluid nozzle. The precursor solution is selected according to the desired final product. The resulting spray flame, due to the reaction between the liquid precursor with the oxygen gas, is stabilized by a surrounding axisymmetrical laminar pilot flame of premixed methane and oxygen gases. A laminar co-flow of nitrogen shields the internal flow against environmental fluctuations and supports the transport of produced particles. The SpraySyn-burner has a simplified geometry for simulations and allows for easy optical access for experiments (Schneider et al., 2019). Therefore, the influence of the combination of liquid precursor solution and gas flow-rates on the composition, size and morphology of produced particles can be investigated.

The objective of the present work is to initially characterize the gaseous velocity field at the nozzle outlet of the SPP1980 SpraySyn-burner, because the flow velocity directly influences the FSP processes, affecting the properties of precursor droplets, flame and ultimately the produced material. To this end, we measured the velocity field from the nozzle outlet to positions located 26 mm downstream of the SpraySyn-burner by means of a hot-wire anemometer and a high-speed 2D-2C PIV at different flow rates under non-reacting (isothermal) and reacting (combustion) conditions.

2 Experimental Setup

In the SpraySyn-burner (Fig. 1a), the liquid precursor solution for the FSP atomization process can be delivered by a 0.70-mm outer-diameter, 0.40-mm inner-diameter needle. The needle is installed in the center of a nozzle with a 1.50-mm outlet diameter, where oxygen flows as dispersion gas. The position and orientation of the needle can be precisely adjusted by three micrometer screws at the burner bottom (not visible in Fig. 1). The needle axis is concentric to the nozzle and its flat tip aligned with the burner surface. A flat-flame from the reaction of a methane-oxygen premixed pilot gas is supported on a porous sintered-brass plate of 70-mm diameter. Nitrogen flows in the outermost annular region as sheath gas to stabilize the flame. It is important to mention that, in the present work, no liquid precursor (or gas) is injected through the needle, so the studied flow can be classified as an annular jet discharged into a co-flowing low-momentum stream.

The gas flow rates are determined by Bronkhorst mass flow controllers (models EL-Flow Select and Mass-Stream) and given in standard conditions of 101325-Pa absolute pressure and 0°C temperature. The gas temperature at the nozzle outlet in non-reacting conditions is 20 ± 3°C measured by a type-K thermocouple connected to a Pico TC-08 data logger.

No combustion chamber is used around the burner, in order to avoid confinement effects in the jet flow. The exhaust gases are collected through a pyramidal chimney hood, located 1 m above the burner surface, and vented out from the lab. The influence of the chimney hood on the flow dynamics is considered negligible at positions close to the burner outlet.

The burner is mounted into a 3D traverse system, which allows its translation with 50-μm resolution for measuring different regions, while hot-wire anemometer or PIV systems are maintained fixed.

A hot-wire anemometer (HWA) is used for validation of PIV data and to measure in regions where no particles can be seeded (i.e., above the porous plate) in non-reacting flows. To this end, a 1D hot-wire 55P16 probe (sensor diameter of 5 μm and length of 1.25 μm) connected to a Dantec Mini-CTA 54T30 system with 12-bit A/D resolution is employed. Since the length of the wire probe acts as a spatial filter, the orientation of the probe is crucial. The probe support is vertically aligned, coinciding with the extension of the PIV plane. The wire probe is orthogonal to the PIV plane in order to increase the sensitivity for the streamwise flow discharged through the burner. The HWA is maintained fixed by a thin horizontal profile to minimise its influence to the surrounding flow. The velocity measurements at different positions are obtained by moving the burner, as described before.

The experimental setup for high-speed two-dimensional two-component PIV measurements (Fig. 1b) is composed of a LaVision HighSpeedStarX camera (1024x1024 pixel, pixel size of 20 μm, 12 bit) equipped with a 200-mm Nikon Nikkor lens with a 532-nm band-pass filter. The light is delivered by a Continuum Mesa Dual-Pulse Nd:YAG laser (2x10 mJ, 532 nm). The light beam is guided by mirrors to the measurement region and the light sheet generated using two spherical lenses and one cylindrical lens. The light sheet is vertical and crosses the central of the burner. A knife-edge filter is used to crop the bottom part of the light sheet, avoiding reflection at the burner surface. Due to the small size of the nozzle, the camera magnification is set to 0.82 and the image width reduced to 640 pixel, leading to a field of view of 15x25 mm, imaging a region from 1 to 26 mm height above the burner (HAB) surface. The acquisition frequency in a traditional dual-frame single-exposure PIV configuration is 5 kHz with a laser pulse delay of 4-10 μs, depending on the flow rate under investigation. The minimum allowable pulse delay of our system is 4 μs. The PIV system is synchronized by a programmable time unit driven by the LaVision DaVis 8.4 software.

The dispersion gas, flowing though a narrow annular slit of 1.50-mm outer and 0.70-mm inner diameter of the nozzle outlet (Fig. 1a), is seeded by titanium-dioxide particles (with nominal diameter of approx. 0.4 μm) using a swirling bed generator with a magnetic stirrer and a bypass. The magnetic stirrer is necessary to increase particle concentration at lower flow rates, while the bypass is used to avoid over seeding at higher flow rates. The particles are dried overnight in an oven at 120°C to decrease moisture and agglomeration. The porosity of the sintered-brass plate does not allow the seeding of the pilot and sheath gases. The seeding through this narrow annular slit is a challenging task. The annular slit is constantly cleaned before each experimental run in order to avoid nozzle restriction, which could otherwise interfere in the dispersion gas velocity or clog the flow.

3 Hot-Wire Processing

The hot-wire anemometer is operated in a constant wire temperature condition. The wire temperature is maintained at 222°C, employing a standard CTA configuration from Dantec with a Wheatstone bridge of 1:20 and an overheat of 0.72 (Jørgensen, 2005).

The HWA is calibrated inside a wind tunnel located in the Fluid Dynamics and Technical Flows Laboratory (ISUT) with a Pitot-static tube as the velocity reference. The air temperature is about 20°C. A power-law calibration curve (King's law) is employed to convert hot-wire voltages into velocities. The hot-wire velocity uncertainty is estimated as 4% for velocities above 0.2 m/s. Below this velocity level, the HWA measurement values are bias, because the natural convection effect in the heat transfer from the hot wire becomes not negligible compared to the forced convection effect due to the flow (Jørgensen, 2005).

4 PIV Processing

The PIV processing in the present work using the DaVis software will now be described. In order to avoid PIV processing in regions of the acquired images without seeding particles, an algorithmic mask, based on the local standard deviation of grey-level intensity and binary operations, is used. Velocity fields are evaluated by a multi-pass cross-correlation approach. Two initial passes employing interrogation windows of 64x64 pixels with a 2:1 elliptical Gaussian weighting function (main axis along the vertical direction) are adopted, because the streamwise jet flow is vertical and faster than the radial flow. The velocity computation procedure is followed by three passes using interrogation windows of 32x32 pixels with a round Gaussian weighting function and high precision in the last pass. All passes use 50% of overlap, leading to a final grid resolution of 0.4 mm. Spurious vectors are removed based on the universal outlier detection over a 5x5

kernel. No interpolation is adopted to replace removed vectors. The PIV uncertainty is estimated by the Correlation Statistics Method (Wieneke, 2015) implemented in the DaVis software.

5 Results

A variety of combinations of sheath-, pilot- and dispersion-gas flow rates are investigated under non-reacting (NR) and reacting conditions with different fuel-oxidizer proportions (ϕ) and without liquid precursor injection. Table 1 summarizes the studied cases. For example, case 3 refers to a stoichiometric flame (ϕ=1) according to the reaction $CH_4 + 2\ O_2 \rightarrow CO_2 + 2\ H_2O$. Gas flow rates are given in standard litres per minute (slm).

Examples of a PIV particle distribution and velocity-magnitude colour plots with vector arrows are presented in Fig. 2. The horizontal coordinate is aligned with the radial jet direction. Despite the acquired non-uniform particle distributions (Fig. 2a), instantaneous velocity fields with good quality and low amount of spurious vectors are obtained under non-reacting (Fig. 2b) and reacting conditions (Fig. 2c). The particle dispersion displays, on average, a cone-like shape that is narrower for higher dispersion gas velocities. The particle concentration diminishes with axial distance from the nozzle (discharge location), because of dispersion and dilution (due to entrainment of surrounding fluid).

PIV statistics from the nozzle outlet to positions located 26 mm downstream, calculated using more than 4300 velocity fields, will now be discussed. In order to validate the PIV measurements, time-averaged velocity profiles along the radial direction at different heights above the surface of the burner are also measured by means of a hot-wire anemometer for case 1. HWA measurements are performed employing only N_2 gas for pilot, dispersion and sheath flow, in order to preserve the calibration. The nozzle outlet is at atmospheric pressure with a temperature of about 20°C, equivalent to the conditions in the wind tunnel. HWA time-averaged velocity is computed for each radial position with steps of 0.2 mm using 1000 samples acquired with a frequency of 1 kHz.

The comparison of time-averaged velocity profiles from HWA and PIV measurements for case 1 is presented in Fig. 3. PIV uncertainty bars are added on every second point to not overcrowd the graph. Excellent agreement is observed between the velocity measurements by these two techniques at all three heights above the burner. The marginally wider profile of the PIV measurement compared to that of the HWA at 4 mm HAB seems to be a consequence of two effects. The first effect is the spatial filtering of the size of the final interrogation window (around 0.8 mm in the present work). The second effect is the intermittent sampling in this region of high shear, where PIV measurements are not possible when the flow is not seeded (entrainment from the slower pilot-gas flow). A dual-peak velocity profile due to the exit from an annular slit is not observed in this plot. Nevertheless, it is expected to exist at lower heights and then to merge into a one-peak profile similar to that of a single round jet (Ko and Chan, 1978). The jet profile develops into a Gaussian curve for heights greater than 8 mm above the burner (R squared of the curve fit above 0.99), in a zone where the axis of the annular potential core is merged to the the nozzle axis (Ko and Chan, 1978). The Gaussian shape of the averaged velocity profile is expected for the developed region of a round jet (Hussein et al., 1994; Pope, 2000). The increase of PIV uncertainties with the radial distance from the jet center is also noticeable in this figure. This is caused probably by the lower amount of velocity vectors to compute the average in these regions, due to the oscillation of the seeded jet border (given by the algorithmic mask employed), and by the low particle number in the corresponding interrogation windows, due to outer fluid entrainment without seeding particles.

Time-average and standard deviation of velocity fields measured by PIV for non-reacting and reacting conditions of cases 1, 2 and 3 are displayed in Fig. 4. The change in the velocity dynamics is enormous due to expansion of the gases during the combustion process. The maximum measured velocity for the non-reacting case is about 58 m/s (Fig. 4a), while for the reacting case with fuel-oxidizer proportion of ϕ=0.5 (Fig. 4b) it is 40% faster and with ϕ=1 (Fig. 4c) it is 47% faster. The higher velocity values appear at the centreline of the jet, as expected for a round jet (Pope, 2000). The velocity fluctuations are also greater under the reacting conditions. For instance, the maximum standard deviation value of reacting flow with ϕ=1 (Fig. 4f) is about 22% greater than for the non-reacting flow (Fig. 4d). Standard deviation values are greatest at radial positions about -1.3 and 1.3 mm. Small differences from the jet symmetry for time-average and standard deviation of velocity fields seem to be caused by a slight misalignment between the nozzle and needle axes.

Fig. 5 shows the difference between non-reacting and reacting conditions of cases 4 and 5 in the measured time-average and standard deviation of velocity fields. Again, pronounced effects in the velocity dynamics are observed during the combustion process. The maximum measured velocity under reacting

Table 1: PIV cases.

		Case 1 NR	Case 2 ϕ=0.5	Case 3 ϕ=1	Case 4 NR	Case 5 ϕ=0.25	Case 6 NR	Case 7 ϕ=0.25
Pilot O_2	[slm]	7.5	6	5	18	16	18	16
Pilot CH_4	[slm]	0	1.5	2.5	0	2	0	2
Dispersion O_2	[slm]	4	4	4	4	4	10	10
Sheath N_2	[slm]	120	120	120	120	120	120	120

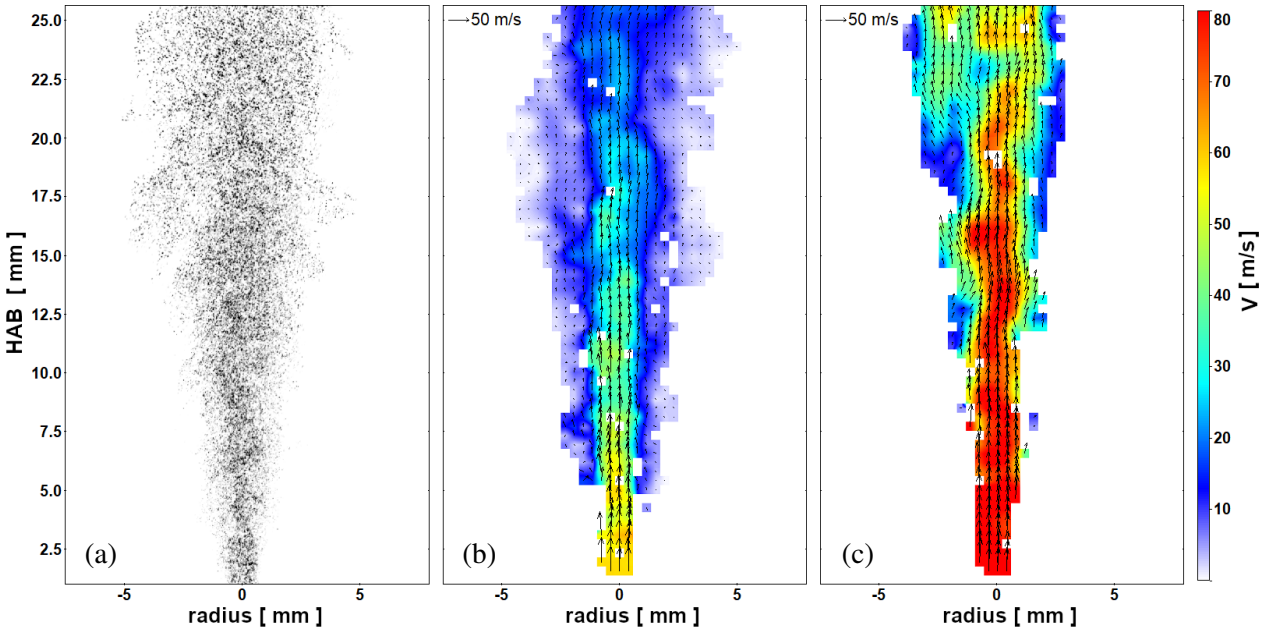

Figure 2: (a) Sample of a typical particle distribution, and instantaneous velocity fields at the nozzle outlet for (b) non-reacting (case 1) and (c) reacting conditions (case 3).

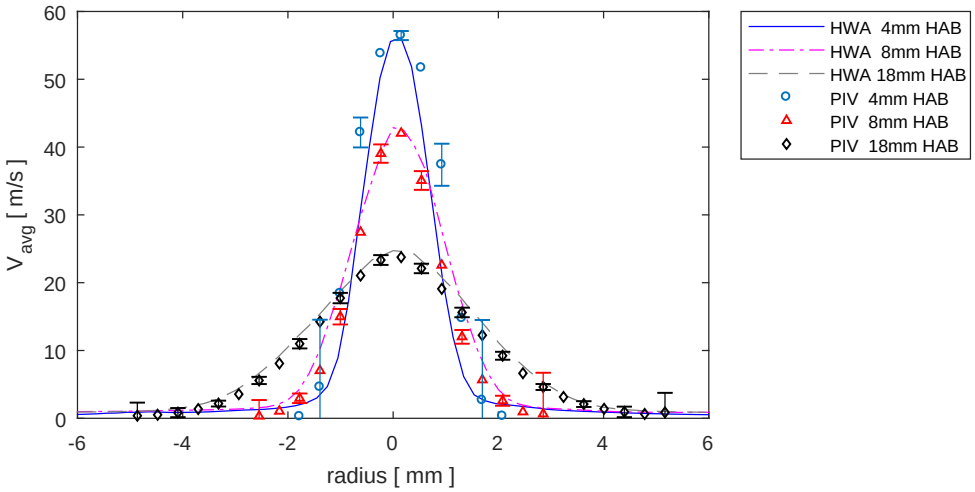

Figure 3: Time-averaged velocity profiles measured by hot-wire anemometer and PIV at different heights above the burner for the non-reacting flow of case 1.

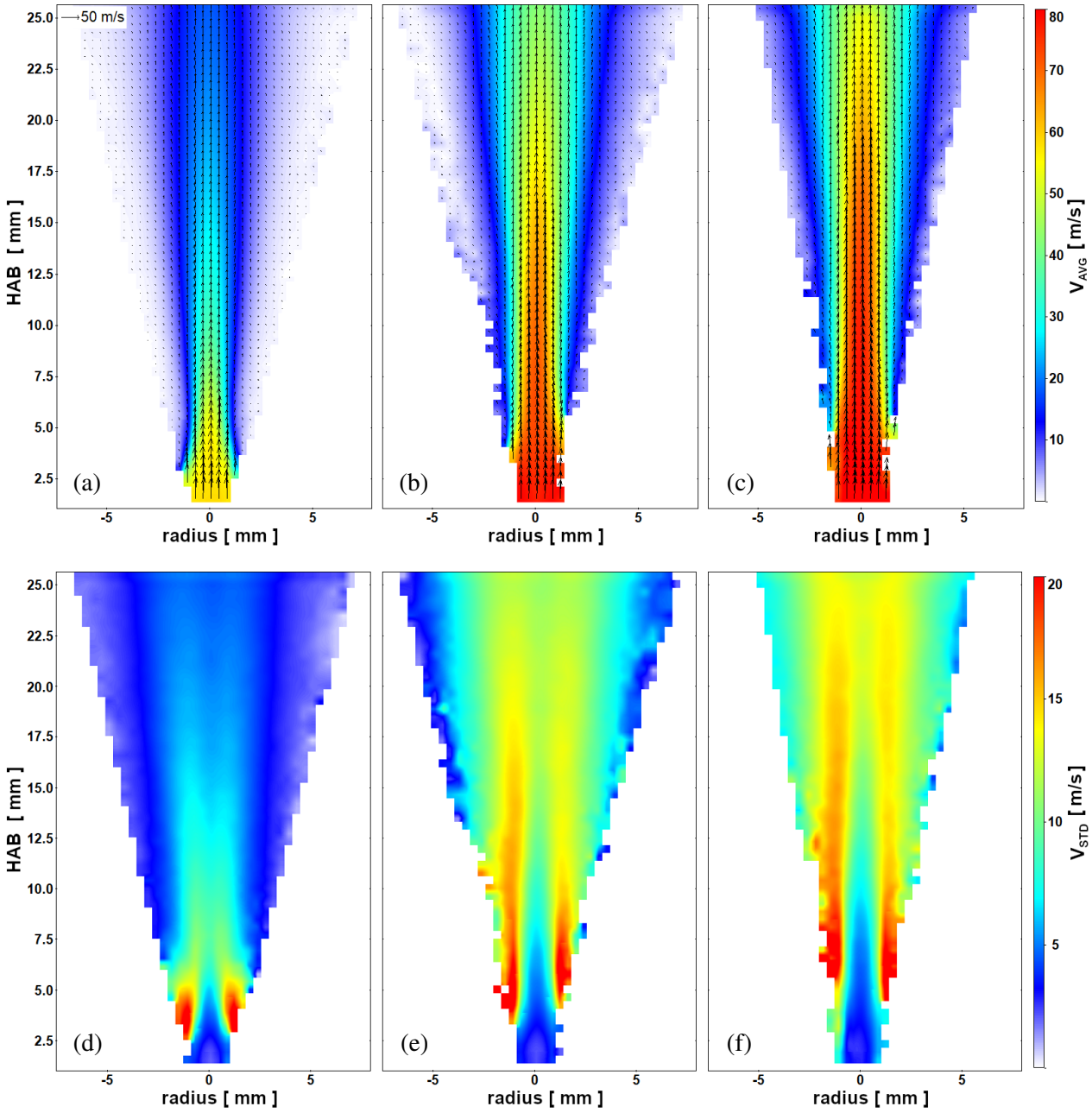

Figure 4: Comparison of non-reacting and reacting conditions at combined flow rates of 120 slm of sheath gas, 7.5 slm of pilot gas and 4 slm of dispersion gas. Time-average (top) and standard deviation of velocity fields (bottom) at the nozzle outlet for cases 1, 2 and 3 (from left to right).

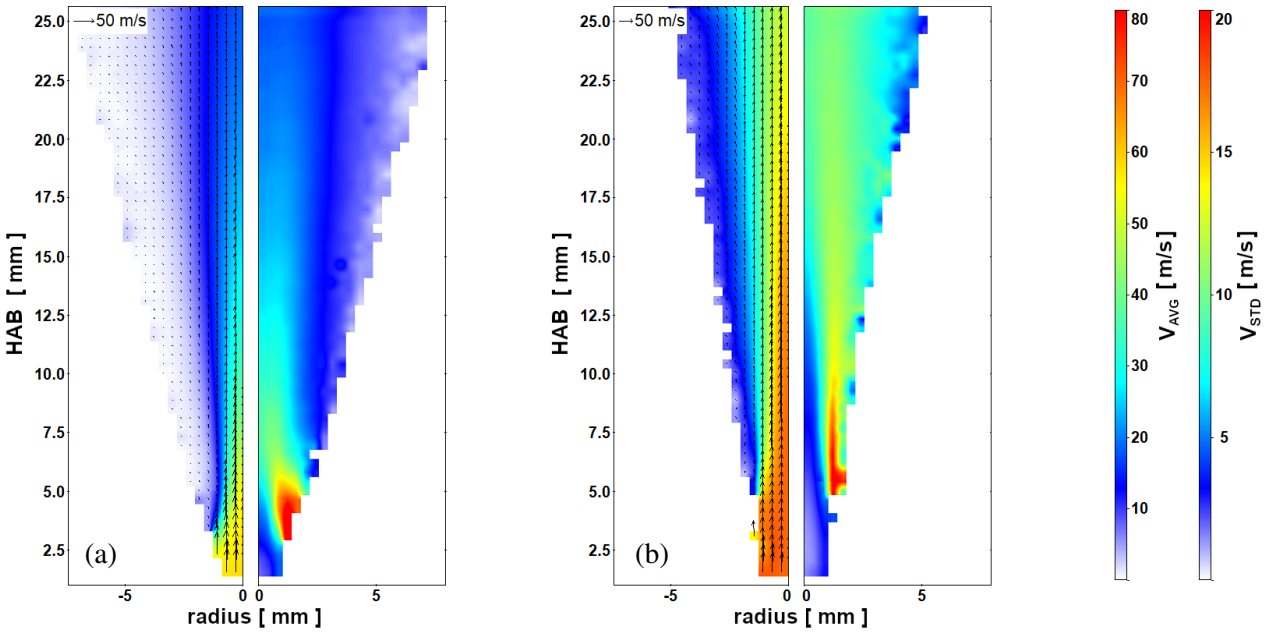

Figure 5: Time-average (left chart region) and standard deviation of velocity fields (right chart region) at the nozzle outlet for (a) non-reacting (case 4) and (b) reacting conditions (case 5) at combined flow rates of 120 slm of sheath gas, 18 slm of pilot gas and 4 slm of dispersion gas.

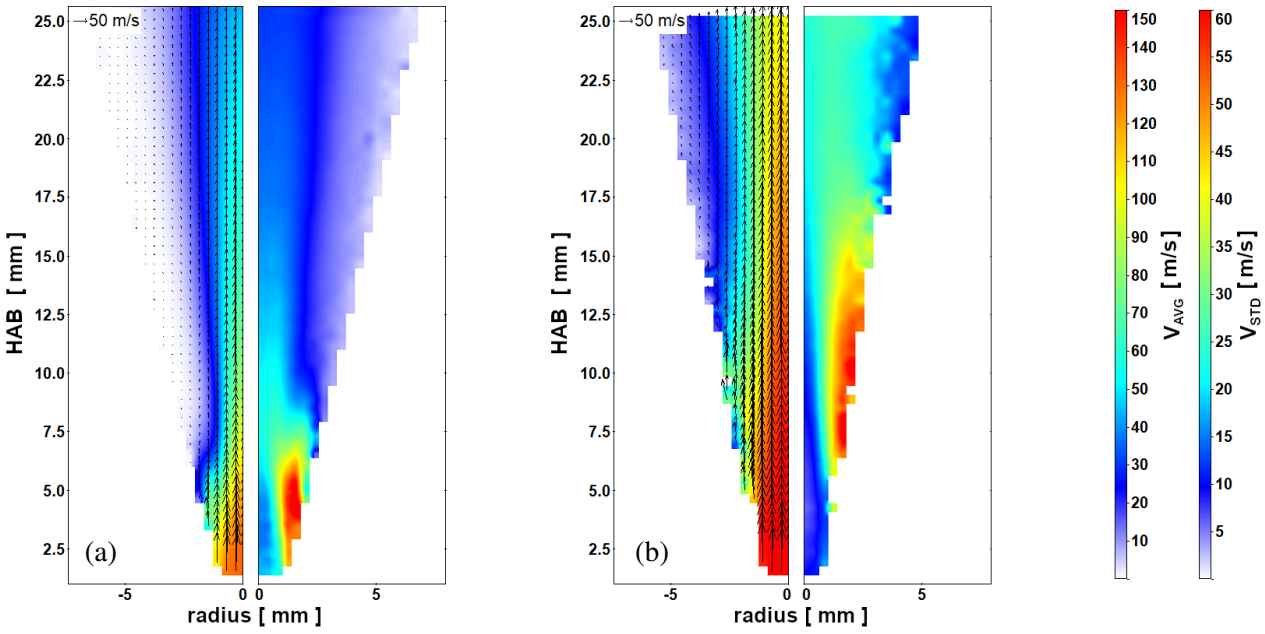

Figure 6: Time-average (left chart region) and standard deviation of velocity fields (right chart region) at the nozzle outlet for (a) non-reacting (case 6) and (b) reacting conditions (case 7) at combined flow rates of 120 slm of sheath gas, 18 slm of pilot gas and 10 slm of dispersion gas.

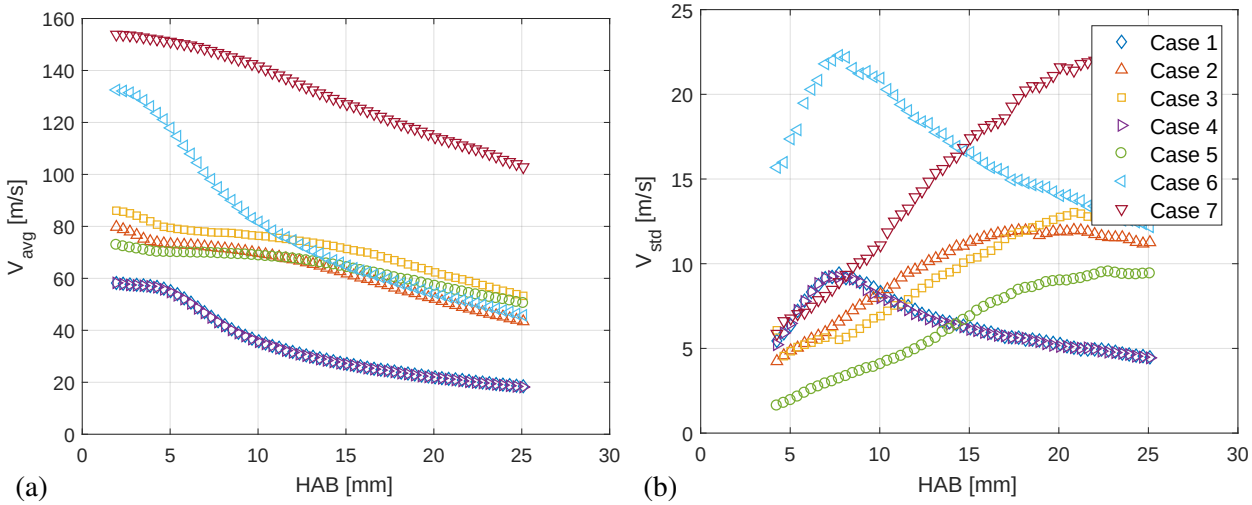

Figure 7: Magnitude profiles of (a) time-average and (b) standard deviation of velocity along the jet centreline under non-reacting and reacting conditions.

flow conditions with ϕ=0.25 is increased by 26% when compared to the non-reacting case. It is interesting to note that negligible differences are observed in the non-reacting case after a 2.4-fold increase of the pilot-gas flow rate, from 7.5 slm (case 1, Fig. 4a,d) to 18 slm (case 4, Fig. 5a).

Time-average and standard deviation of velocity fields under non-reacting and reacting conditions of cases 6 and 7 are presented in Fig. 6. Case 7 is the current standard condition recommended to operate the SPP1980 SpraySyn-burner according to Schneider et al. (2019). The maximum measured velocity in the reacting flow (Fig. 6b) is 16% greater than that of the non-reacting corresponding flow (Fig. 6a). Comparing this figure with Fig. 5, we can observe that the increase of dispersion-gas flow rate, not only changes the measured averaged velocity fields (expected behaviour), but also the standard deviation velocity fields. For instance, the maximum velocity under reacting conditions of case 7 (Fig. 6b) is 2-fold greater than that of case 5 (Fig. 5b), while the maximum velocity fluctuation is 3.4-fold increased.

Centreline profiles of the magnitude of time-averaged velocity and of their fluctuations are presented in Fig. 7. The legend for both graphs is displayed in Fig. 7b. Significant differences in the shape and in the magnitude values are observed in both plots comparing associated flows under non-reacting and reacting conditions (i.e., case 1 compared with case 2 or 3, case 4 compared with 5, and case 6 with 7). The profile peaks of the standard deviation of velocity are always located at positions further downstream under reacting conditions. In contrast, no difference is observed neither in the magnitude of the time-averaged velocity nor in its standard deviation between non-reacting cases 1 and 4 (same dispersion gas flow rate). The jet flow close to the burner therefore seems to be independent of the low-momentum pilot gas flow rate under the non-reacting conditions of the present work. This fact was already discussed for the visual inspection of the associated 2D velocity fields of Fig. 4a and 5a.

6 Conclusions

The present work characterizes the gaseous velocity field from the nozzle outlet to positions located 26 mm downstream of the SPP1980 SpraySyn-burner by means of 2D-2C PIV at various flow rates for non-reacting and reacting conditions. Time-average and standard deviations of velocity fields are discussed. The PIV velocity field is validated against hot-wire anemometer measurements under non-reacting condition, showing good agreement. The quality of the present measurements are corroborated by the computed low uncertainty levels.

Regarding the flow velocity dynamics, great changes are observed comparing non-reacting and reacting cases, and also comparing reacting cases with different fuel-oxidizer proportions (stoichiometry), due to temperature change and expansion of the gases during the combustion process. Peaks of the standard deviation of velocity along the jet centreline are located at positions further downstream under reacting conditions.

The understanding of the dispersion gas flow field provided here is an important step, because the flow velocity is directly linked to the flame spray pyrolysis processes, affecting the precursor atomization, flame and ultimately the size and morphology of the produced material.

Acknowledgements

The authors gratefully acknowledge the funding by the German Research Foundation (DFG) within the priority program 'Nanoparticle Synthesis in Spray Flames SpraySyn: Measurement, Simulation, Processes' (SPP1980). We thank Dr.-Ing. Katharina Zähringer, from Fluid Dynamics and Technical Flows Laboratory (ISUT), for lending the hot-wire-anemometer system. Florian Schneider and Samer Suleiman, from the Institute for Combustion and Gas Dynamics - Reactive Fluids (Duisburg-Essen University), and Dr.-Ing. Gunar Boye, from Technical Thermodynamics Laboratory (ISUT), are also acknowledged.

References

Abdelsamie A and Thévenin D (2019) On the behavior of spray combustion in a turbulent spatially-evolving jet investigated by direct numerical simulation. *Proceedings of the Combustion Institute* 37:3373–3382

Gurav A, Kodas T, Pluym T, and Xiong Y (1993) Aerosol processing of materials. *Aerosol science and technology* 19:411–452

Hussein HJ, Capp SP, and George WK (1994) Velocity measurements in a high-reynolds-number, momentum-conserving, axisymmetric, turbulent jet. *Journal of Fluid Mechanics* 258:31–75

Jørgensen FE (2005) *How to measure turbulence with hot-wire anemometers: a practical guide*. Dantec dynamics

Kilian D, Engel S, Borsdorf B, Gao Y, Kögler A, Kobler S, Seeger T, Will S, Leipertz A, and Peukert W (2014) Spatially resolved flame zone classification of a flame spray nanoparticle synthesis process by combining different optical techniques. *Journal of Aerosol Science* 69:82–97

Ko N and Chan W (1978) Similarity in the initial region of annular jets: three configurations. *Journal of Fluid Mechanics* 84:641–656

Menser J, Kluge S, Wiggers H, Dreier T, and Schulz C (2014) Approach to standardize a spray-flame nanoparticle synthesis burner. in *Int. Workshop on Laser-induced Incandescence, Hven, Sweden*

Messing GL, Zhang SC, and Jayanthi GV (1993) Ceramic powder synthesis by spray pyrolysis. *Journal of the American Ceramic Society* 76:2707–2726

Mueller R, Mädler L, and Pratsinis SE (2003) Nanoparticle synthesis at high production rates by flame spray pyrolysis. *Chemical Engineering Science* 58:1969–1976

Okuyama K and Lenggoro IW (2003) Preparation of nanoparticles via spray route. *Chemical engineering science* 58:537–547

Pope SB (2000) *Turbulent flows*. Cambridge University Press, Cornell University, New York. 1 edition

Schneider F, Suleiman S, Menser J, Borukhovich E, Wlokas I, Kempf A, Wiggers H, and Schulz C (2019) Spraysyn a standardized burner configuration for nanoparticle synthesis in spray flames. *Rev Sci Instrum (submitted)*

Schulz C, Dreier T, Fikri M, and Wiggers H (2018) Gas-phase synthesis of functional nanomaterials: challenges to kinetics, diagnostics, and process development. *Proceedings of the Combustion Institute* 37:83–108

Strobel R and Pratsinis SE (2007) Flame aerosol synthesis of smart nanostructured materials. *Journal of Materials Chemistry* 17:4743–4756

Wieneke B (2015) PIV uncertainty quantification from correlation statistics. *Measurement Science and Technology* 26:074002